BULLETIN OF THE POLISH ACADEMY OF SCIENCES
TECHNICAL SCIENCES, Vol. 67, No. 3, 2019
DOI: 10.24425/bpasts.2019.129661

Calculations of transport parameters in semiconductor superlattices based on the Greens' functions method in different Hamiltonian representations

M. MĄCZKA* and G. HAŁDAŚ

Department of Electronics Fundamentals, Rzeszów University of Technology, W. Pola 2, 35-959 Rzeszów, Poland

Abstract. Two methods for calculating transport parameters in semiconductor superlattices by applying Green's functions are compared in the paper. For one of the methods, the Wannier functions method, where computations in the complex space and Wannier functions base are required, the Hamiltonian matrix is small in size and its elements depend solely on the energy. For the real space method, as it operates in the floating point domain and uses the Hamiltonian containing the elements dependent both on energy and position, the Hamiltonian matrix is larger in size. The size makes the method computationally challenging. To find the consequences of choosing one of the methods, a direct comparison between the computations, obtained for both methods with the same input parameters, was undertaken. The differences between the results are shown and explained. Selected simulations allowed us to discuss advantages and disadvantages of both methods. The calculations include transport parameters such as the density of states and the occupation functions, with regard to scattering processes where the self-consistent Born approximation was used, as well as the spatial distribution of electron concentration for two superlattices structures. The numerical results are obtained within the non-equilibrium Green's functions formalism by solving the Dyson and the Keldysh equations.

Key words: semiconductor superlattice, NEGF formalism, Wannier functions.

1. Introduction

Semiconductor superlattices (SL) are the base structures for quantum cascade lasers (QCLs). They are the devices that emit radiation in the mid- to far-infrared electromagnetic spectrum [1–3]. The concept of the process for lasing in QCLs had been proposed by R.F. Kazarinov and R.A. Suris [4] and over the last two decades they inspired many scientific and practical studies: the works [5–6] deserve particular attention. Theoretical approach to transport in superlattices brought many interesting works on the application of the Monte Carlo method [7–8]. With increasing computing power, the method has gained gravity. Still, it is worth to remember that Monte Carlo simulations base on semi-classical method of Boltzmann equation, in which neglect quantum coherence. Yet, their uncertainty can be verified with other computational methods, some of which are: Green's functions method operating in the real space [9] (that is the approach we adopted) or maximally localized Wannier functions (MLWF) applied to calculation by Wacker et al. [10–13]. These methods provide software tools for simulating nanodevices, e.g, a widely known Nextnano [14]. The tools are used to explore physical phenomena in superlattices or to design specific parameters of the devices. Simulations can be found surprising at times, both with regard to the variety of values the calculated parameters take, and the time required to obtain final results. Therefore, it might be difficult to evaluate the effectiveness and the correctness of the results, as the main features of the numerical models applied are not known. Despite many discussions on advantages and disadvantages of various approaches, the key question, which method to select to obtain quick, results accurate for a particular case, has remained unsolved. It seems quite reasonable to assume that the analysis of the results obtained for both methods with identical input parameters can shed at least some light on the problem. As for a commercial user, it can prove difficult, time-consuming, and costly to select proper testing tools, the analysis we propose helps to take the right decision on the method and the tool to be applied.

The present study is a detailed comparison of two methods to calculating the transport parameters in SL, where non-equilibrium Green's function (NEGF) theory is applied. As for the first method, presented by Hałdaś et al. [15–16] and Kolek et al. [17], the computations are performed in the real space, we call it the real space method (RSM). Although this approach provides accurate data for many device parameters, it requires huge data storage capacities. For the other method, presented by Mączka et al. [18–22] where the Wannier functions (WF) properties for superlattices are applied, called the Wannier functions method (WFM), the main computations are limited to the energy space. For such a case a nano-device can be described with a small-size Hamiltonian, hence simulations are much faster than RSM ones. For biased SL structures, the transformation of quantum states from position to energy domain is required, therefore WFM may be questioned with regard to their accuracy. We have also addressed this problem. It has been shown that the

*e-mail: mmaczka@prz.edu.pl

Manuscript submitted 2018-04-24, revised 2018-07-09, initially accepted for publication 2018-08-09, published in June 2019.

results obtained for both approaches may differ, and the respective causes have been explained. The analysis is limited to the basic functions associated with the SL transportation, as we believe any other differences in parameters may be a direct consequence of the changes presented here.

2. Main features of the models

In the paper, two SL structures are considered. First of them (*structure A*) is a base of typical far-infrared terahertz QCL, described by Callebaut et al. [23]. In each QCL structure, the period contains an active region and a separate injector region. The lasing transition occurs in the active region. The injector serves as a reservoir of electrons to be injected into the active region of the adjacent stage. The direction of the electron flow is shown in Fig. 1. Electrons are injected from $n = 1$' into $n = 5$ (in the next period) to make a subsequent vertical transition into $n = 4$. LO phonon transition occurs between levels $n = 4$, $n = 3$ and $n = 2$, $n = 1$. It is viable as the subbands $n = 4$ and $n = 3$ are resonant and the distance between these states is above the LO phonon energy. As shown in Fig. 1, the electron flow resembles a cascade formed by the electrons moving from one stage to the other, as long as a bias is applied.

The second of considered SL structures (*structure B*) was described by Page et al. [24]. It is room temperature 25 mW pulsed operation of an AlGaAs/GaAs mid-infrared ($\sim$9.5 μm) QCL structure.

Two models simulating phenomena in SL were applied in our computations. For the WFM, a model (see Fig. 2a) is composed of the infinite number of modules. One module corresponds to one period of the SL structure.

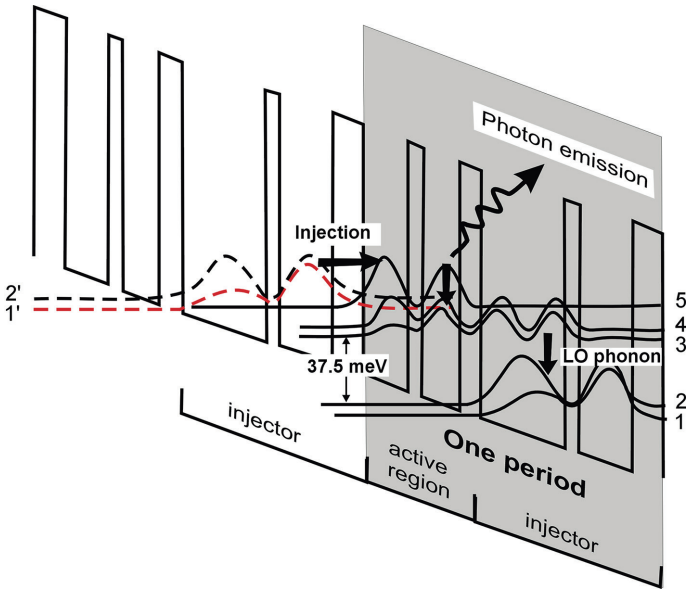

Fig. 1. Conduction-band line-up for the first of concerned SL structure. The device consists of GaAs/$Al_{0.15}Ga_{0.85}As$ layers of thicknesses of 7.8/**2.4**/6.4/**3.8**/<u>14.8</u>/**2.4**/9.4/**5.4** nm; the barriers are marked in boldface, wells in plain text; underlined value is doped to $n = 1.93\times10^{16}$ cm^{-2} in the 14.8 nm wide well. The arrows indicate transitions between the quantum states

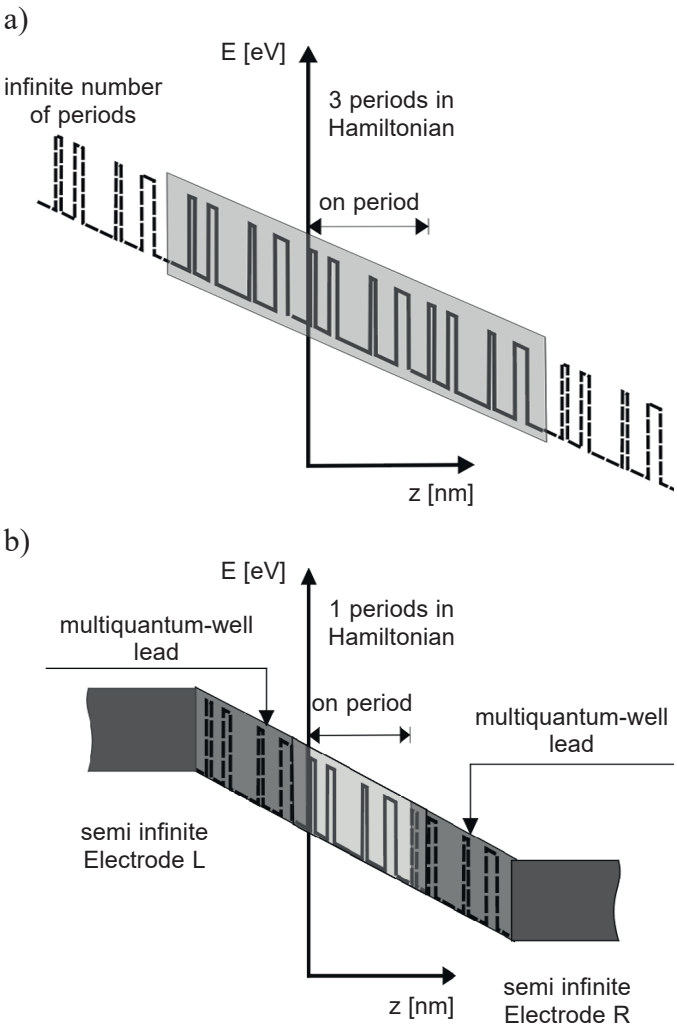

Fig. 2. Two models of superlattice structures: a) The model used in WFM, which comprises an infinite number of modules (one module provides one SL structure period); b) The multi-quantum well model used in RSM

For such an infinite model, the allowed minibands and Bloch functions are initially determined. A one-dimensional Schrödinger equation

$$\left[\frac{-\hbar^2}{2}\frac{d}{dz}\frac{1}{m_e(z)}\frac{d}{dz} + V(z) + \frac{\hbar^2 k^2}{m_e(z)}\right]\Psi(z) = E\Psi(z), \qquad (1)$$

where $\Psi(z)$ are envelope functions, $V(z)$ is the spatially dependent superlattice potential, and $m_e(z)$ is the effective mass constant within each semiconductor layer, is required to be solved.

Equation (1) is solved by the transfer matrix formulation (TMF) method [19]. In this approach, the envelope function $\Psi(z)$ in the semiconductor layer j can be written as

$$\psi_j(z) = A_j e^{ik_j(E)(z-z_j)} + B_j e^{ik_j(E)(z-z_j)}, \tag{2}$$

where z_j is the position of the structure region j, and $k_j(E) = \sqrt{2m_j(E-V_j)/\hbar^2}$, with m_j and V_j as the mass and the potential in the region j, respectively. Subsequently, the Bloch states in equation (2) are computed. They are denoted as $\varphi_q^{\nu}(z)$, where n is the index of the miniband and q is the Bloch vector within the range $\langle -\pi/d, \pi/d \rangle$. The term d is the length of the superlattice period. The Bloch functions are evaluated by the grid with 0.1 nm mesh size (a). It yields 524 points per period. As in our case one miniband for excited state is included, the miniband index ν runs from 1 to 5. Then, quantum states are constructed on the basis of MLWF. The Wannier functions associated with miniband ν are constructed according to the relation [25]

$$W^{\nu}(z-nd) = \sqrt{\frac{d}{2\pi}} \int_{-\pi/d}^{\pi/d} \varphi_q^{\nu}(z) \cdot e^{-inqd} dq. \tag{3}$$

The phases of the Bloch functions are chosen arbitrarily for each value of q to obtain MLWF. These operations were performed for each miniband ν. Practically, a separate numerical method is required to analyze WF localization. We based it on the analysis of the WF parts maxima, the real and imaginary alike. The second criterion is to check the values of WF integrals in the selected potential wells of the SL structure. The results of the numerical research were reported in [19, 21]. Quantum states, obtained as above, are necessary to construct the Hamiltonian matrix and to apply the NEGF formalism, as explained further.

The model applied in RSM (see Fig. 2b) is a semi-infinite model, in which the multi-quantum well alignment [15] of the biased SL band structure continues into the leads (semi-infinite electrodes R and L). It is assumed that outside the analyzed part of the structure, the conduction band edge does not change. It is the main difference for this model with respect to the WMF, as it does not require initial computations of the allowed minibands in the simulated structure. Unlike WFM, the quantum states in SL can be obtained directly by employing NEGF formalism.

3. Hamiltonians for WFM and RSM

The Wannier states, obtained as presented in the previous section, are used to construct the Hamiltonian $\hat{H}_{WFM}$. In our simulations, only the couplings between the Wannier states in the same period, and the nearest-neighbor periods are considered. Therefore, the matrices representing the Hamiltonian are constructed with 15 states from three periods, what corresponds to basic assumptions proposed in [13].

The Hamiltonian $\hat{H}_{WFM}$ may be separated into two parts: $\hat{H}_{WFM} = \hat{H}_0 + \hat{H}_{scatt}$, where $\hat{H}_{scatt}$ represents the scattering processes in the investigated structure, whereas $\hat{H}_0$ contains the superlattice potential and the static electric field ξ applied in the growth direction, thus rewritten as $\hat{H}_0 = \hat{H}_{SL} + \hat{H}_{\xi}$. By expressing the Hamiltonian $\hat{H}_{SL}$ in the Wannier basis, we obtain [25]

$$\mathbf{H}_{SL} = \sum_{n,\nu} \sum_{\mathbf{k}} \left[\begin{array}{l} E_{\nu\mathbf{k}} \hat{a}_{\mathrm{n},\mathbf{k}}^{\nu\dagger} \hat{a}_{\mathrm{n},\mathbf{k}}^{\nu} + \\ + T_1^{\nu} \left(\hat{a}_{\mathrm{n+1},\mathbf{k}}^{\nu\dagger} \hat{a}_{\mathrm{n},\mathbf{k}}^{\nu} + \hat{a}_{\mathrm{n-1},\mathbf{k}}^{\nu\dagger} \hat{a}_{\mathrm{n},\mathbf{k}}^{\nu} \right) \end{array} \right], \tag{4}$$

where n is the number of the superlattice periods, index ν labels the Wannier state $W_n^{\nu}(z)$ within the period n, $\hat{a}_{\mathrm{n},\mathrm{k}}^{\nu\dagger}$ and $\hat{a}_{\mathrm{n},\mathrm{k}}^{\nu}$ stand for the creation and annihilation operators for an electron with in-plane wave vector **k.** Parameter T_1^{ν} represents the off-diagonal couplings between Wannier levels in different periods, and $E_{\nu\mathrm{k}}$ are the diagonal elements of $\mathbf{H}_{SL}$ in this basis. The Hamiltonian $\hat{H}_{\xi}$ can be written as [25]

$$\mathbf{H}_{\xi} = \sum_{\mathrm{n},\mu,\nu} \sum_{\mathbf{k}} \left\{ \begin{array}{l} -e\xi R_0^{\mu\nu} \hat{a}_{\mathrm{n},\mathbf{k}}^{\nu\dagger} \hat{a}_{\mathrm{n},\mathbf{k}}^{\nu} + \\ -ne\xi d\delta_{\mu\nu} \hat{a}_{\mathrm{n},\mathbf{k}}^{\nu\dagger} \hat{a}_{\mathrm{n},\mathbf{k}}^{\nu} + \\ -e\xi R_1^{\mu\nu} \left[\hat{a}_{\mathrm{n+1},\mathbf{k}}^{\nu\dagger} \hat{a}_{\mathrm{n},\mathbf{k}}^{\nu} + \hat{a}_{\mathrm{n-1},\mathbf{k}}^{\nu\dagger} \hat{a}_{\mathrm{n},\mathbf{k}}^{\nu} \right] \end{array} \right\}, \tag{5}$$

where d is the length of a period, e is the electron charge, and $R_l^{\mu\nu} = \int dz W^{\mu^*}(z-ld) z W^{\nu}(z)$. In the NEGF theory, scattering processes expressed in $\hat{H}_{scatt}$ are applied in the form of self-energies, described in the next section. For the single energy of the wave vector **k**, the size of Hamiltonian matrix in WFM can be calculated from the formula $S_{H_{WFM}} = N_P \cdot N_{WS}$, where N_P is the number of analyzed periods, and N_{WS} is the number of Wannier states, in the specified range of energy. Three periods with five Wannier states each are considered, thus (for *structure A*) the resulting size of the Hamiltonian matrix $S_{H_{WFM}}$ is 15. The Hamiltonian of the device, used for real space method, can be written as [25]

$$\mathbf{H}_{RSM} = \sum_{z} \sum_{\mathbf{k}} \left[\begin{array}{l} -(E_{Cz} + V_z + E_{\mathbf{k}}) \hat{a}_{\mathrm{z},\mathbf{k}}^{\nu\dagger} \hat{a}_{\mathrm{z},\mathbf{k}}^{\nu} + \\ -t \left(\hat{a}_{\mathrm{z+1},\mathbf{k}}^{\nu\dagger} \hat{a}_{\mathrm{z},\mathbf{k}}^{\nu} + \hat{a}_{\mathrm{z-1},\mathbf{k}}^{\nu\dagger} \hat{a}_{\mathrm{z},\mathbf{k}}^{\nu} \right) \end{array} \right], \tag{6}$$

where z is the spatial coordinate in the growth direction for the energy states E, V is the Hartree potential, and m is the position and energy-dependent effective mass. The grid with $a = 0.6$ nm for z space coordinate is assumed, hence the size of the Hamiltonian matrix for a single energy level of the wave vector **k**, can be defined as $S_{H_{RSM}} = d/a$. For this method, we consider one period of the superlattice, the size of the Hamiltonian matrix $S_{H_{RSM}}$ is 88 (for *structure A*). The way, in which the Hamiltonian matrix is constructed, as well as its content, provides the basic difference between two presented methods.

$\mathbf{H}_{RSM}$ contains elements, which depend both on energy and position, therefore many parameters of the SL structure can be calculated directly from the RSM. On the other hand, when comparing the size of the Hamiltonian matrices, it seems that under the NEGF formalism, where the same equations are solved for both methods, the calculations with WFM should be faster than with RSM. Still, as WFM requires to be computed prior to MLWF, it is not so obvious. Both methods, applied to SL simulations with the same parameters, are presented in order to resolve such doubts.

4. Green's functions and self-energies

While computing transport characteristics in the SL structure under the applied bias, the first step is to describe the non-equilibrium stationary state of the system by using non-equilibrium Green's functions namely, the retarded Green's function G^R and the correlation function $G^<$. For both methods, the Dyson and the Keldysh equations [28] are solved. The first of them, in the basic form can be written as [29]

$$\left(E\mathbf{I}-\mathbf{H}-\mathbf{\Sigma}^R\right)\mathbf{G}^R=\mathbf{I}. \tag{7}$$

In this equation, $\mathbf{G}^R$ is the matrix of the retarded Green's functions, which in the Wannier basis takes on the form $G^R_{WF}=f(\alpha,\beta,k_{\|},E)$, where α and β are the general indices that include both the period and the Wannier level indices. For example, $\alpha\equiv\alpha(\mu,n)$, whereas n refers to the superlattice periods and μ corresponds to the selected Wannier levels. The remaining parameters in the relation G^R_{WF} are: the in-plane wave vector $k_{\|}$ and the total energy E.

In the RSM approach, the retarded Green's functions can be written as $G^R_{RS}=f(z,z',k_{\|},E)$, where z and z' are the real space coordinates.

The Hamiltonian equations in WFM and RSM are presented in section 3. The main difference between the Hamiltonians is the reduced number of the position coordinates for WFM. Consequently, the Hamiltonian matrix size is significantly smaller, so simulations take shorter time. To illustrate the time efficiency of simulations, we initially assumed the self-energies $\mathbf{\Sigma}^R$ as the constant diagonal elements $i\eta$ for both described methods. The parameter η was used as defined with [30]

$$G^R(E)=\lim_{\eta\to 0^+}G(Z=E+i\eta). \tag{8}$$

The correlation function $G^<$ was calculated from the Keldysh equation [31]

$$\mathbf{G}^<=\mathbf{G}^R\mathbf{\Sigma}^<\mathbf{G}^{R\dagger}, \tag{9}$$

where the self-energies $\mathbf{\Sigma}^<$ initially (in thermodynamic equilibrium) are the diagonal elements $i\eta\cdot f_n(E)$, where

$$f_n(E)=1\Big/\left[\exp\left((E-E_F)/k_BT\right)-1\right]. \tag{10}$$

For the biased structure

$$f_n(E)=1\Big/\left[\exp\left((E-\mu_{zB})/k_BT\right)-1\right], \tag{11}$$

where the values of μ_{zB} were determined from approximation inspired by Büttiker probes [32, 33]. A detailed description of using this approach in our simulations, was provided in [21, 22].

Then, the self-consistent Born approximation was initiated. According to this approach, in the WFM the self-energies $\sum^R_{WF}(\alpha,\beta,k_{\|},E)$ are evaluated with the formula [12]

$$\sum\nolimits^{R,ph}_{WF,\alpha_1\alpha_1,\mathbf{k}}(E)=\sum_{\beta,\mathbf{k}'}\left|V^{ph}_{\alpha_1\beta}(\mathbf{k},\mathbf{k}')\right|^2 \times\left\{\begin{array}{l}\left[f_B(E_{lo})+1\right]G^R_{\beta\beta,\mathbf{k}'}(E-E_{lo})+\\+f_B(E_{lo})G^R_{\beta\beta,\mathbf{k}'}(E+E_{lo})+\\+\frac{1}{2}\left[G^<_{\beta\beta,\mathbf{k}'}(E-E_{lo})-G^<_{\beta\beta,\mathbf{k}'}(E+E_{lo})\right]+\\+i\int\frac{dE_1}{2\pi}\left\{\begin{array}{l}G^<_{\beta\beta,\mathbf{k}'}(E-E_1)\times\\\left(P\left\{\frac{1}{E_1-E_{lo}}\right\}-P\left\{\frac{1}{E_1+E_{lo}}\right\}\right)\end{array}\right.\end{array}\right\}, \tag{12}$$

where E_{lo} is the energy of the optical phonons, and $f_B(E)=1/\left[\exp(E/k_BT)-1\right]$ is the equilibrium phonon distribution at temperature T. The matrix elements $V^{ph}_{\alpha_1\beta}(\mathbf{k},\mathbf{k}')$ represent the interaction with optical phonons and can be calculated according to equation [12]

$$\left|V^{ph}_{\alpha_1\beta}(\mathbf{k},\mathbf{k}')\right|^2=2\pi C\int_{-\infty}^{+\infty}dq_z\left\{\begin{array}{l}\left|M_{\alpha\beta}(q_z)\right|^2\\\times\left\{\begin{array}{l}\frac{1}{\sqrt{B\cdot 4kk'}}+\\-\frac{q_0B}{\sqrt{B\cdot 4kk'}}\end{array}\right.\end{array}\right\}, \tag{13}$$

where the constant value $C=E_{lo}e^2\left[n(\omega_{lo})+1/2\pm 1/2\right]/4\pi\varepsilon_p$ with E_{lo} as the LO-phonon energy (36.7 meV), ε_p as the relative permittivity of the material and $n(\omega_{lo})$ is a phonon number state represented by $f_B(E_{lo})$. The expression $M_{\alpha\beta}(q_z)$ is computed according to [12]

$$M_{\alpha\beta}(q_z)=\int_0^{L_w}dz\,e^{\mp iq_zz}W^*_\alpha(z)\cdot W_\beta(z), \tag{14}$$

where L_w is the distance along the z-direction, over which the Wannier functions $W(z)$ extend. The parameter B in equation (13) replaces the relation $B=\left(q_z^2+k^2+k'^2+q_0^2\right)$ where q_0 is the Debye length and q_z is the component of the Bloch vector in the growth direction. The self-energies in the Keldysh equation $\sum^<_{WF}(\alpha,\beta,k_{\|},E)$ can be written as [12]

$$\sum\nolimits^{<,ph}_{\alpha_1\alpha_1,\mathbf{k}}(E)=\sum_{\beta,\mathbf{k}'}\left|\mathbf{V}^{ph}_{\alpha_1\beta}(\mathbf{k},\mathbf{k}')\right|^2\times\left\{\begin{array}{l}f_B(E_{lo})\cdot\mathbf{G}^<_{\beta\beta,\mathbf{k}'}(E-E_{lo})+\\+\left[f_B(E_{lo})+1\right]\cdot\mathbf{G}^<_{\beta\beta,\mathbf{k}'}(E+E_{lo})\end{array}\right\}. \tag{15}$$

In the real space method, the self-energies $\sum^R_{RS}(z,z',k_{\|},E)$ are evaluated as [27]

$$\sum_{RS}^{R,ph}(z,z',k_{||},E)=$$

$$=\frac{\gamma}{8\pi^2}\int_{-\infty}^{\infty}dq_z\int dl_{||}\left\{\begin{array}{l}\dfrac{q_{||}^2+q_z^2}{(q_{||}^2+q_z^2+q_0^2)}e^{iq_z(z-z')}\\ \times((f_B+1)G^R(z,z',l_{||},E-E_{lo})\\ +f_BG^R(z,z',l_{||},E+E_{lo})+\\ +\dfrac{1}{2}(G^<(z,z',l_{||},E-E_{lo})+\\ -G^<(z,z',l_{||},E+E_{lo}))+\\ +iP\int\dfrac{dE'}{2\pi}\left(\dfrac{G^<(z,z',l_{||},E')}{E-E'-E_{lo}}+\right.\\ \left.-\dfrac{G^<(z,z',l_{||},E')}{E-E'+E_{lo}}\right)\end{array}\right\},\quad(16)$$

where $\gamma=e^2E_{lo}\left(\varepsilon_\infty^{-1}-\varepsilon_r^{-1}\right)/2\varepsilon_0$ and the self-energies $\sum_{RS}^{<,}(z,z',k_{||},E)$ are described by [26]

$$\sum_{RS}^{<,ph}(z,z',k_{||},E)=$$

$$=\frac{\gamma}{8\pi^2}\int_{-\infty}^{\infty}dq_z\int dl_{||}\left\{\begin{array}{l}\dfrac{q_{||}^2+q_z^2}{(q_{||}^2+q_z^2+q_0^2)}e^{iq_z(z-z')}\\ \times((f_B+1)G^<(z,z',l_{||},E-E_{lo})+\\ +f_BG^<(z,z',l_{||},E+E_{lo}))\end{array}\right\}.\quad(17)$$

To determine the Green's functions, $G^R(\mathrm{E})$ and $G^<(\mathrm{E})$, the quantum transport equations (7, 9) and the equations for the self-energies are solved iteratively, until a self-consistent solution for these equations is reached. Computations stop upon reaching the assumed convergence. The convergence test was carried by comparing differences in the **k**-integrated Green's functions $\mathrm{Im}\left\{G_{\alpha\alpha}^R(E)_{i+1}-G_{\alpha\alpha}^R(E)_i\right\}$ with the carrier density $\mathrm{Im}\left\{G_{\alpha\alpha}^<(E)_{i+1}-G_{\alpha\alpha}^<(E)_i\right\}$, evaluated in two successive iteration steps, with a given tolerance value.

5. Simulations and discussion

Both methods were tested using a standard PC, equipped with an Intel XEON 3.33 GHz. The analysis of simulations starts with comparing of the minibands parameters, calculated for the typical THz-QCL structure [23] (*structure A*) in the thermodynamic equilibrium. The numerical results are presented in Table 1, which shows the values of energy for the five lowest energy levels of the quantum states, obtained directly from the RSM. The other 3 columns of this table present basic parameters of the minibands computed with the TMF method under the applied WFM. Similarly to the approach presented elsewhere [13], a five Wannier states base were used and interactions were limited to three adjacent structural periods. Therefore, in TMF part of Table 1, the values of the energy levels for five lowest centers of the minibands and the corresponding values of T_1^v, representing the coupling between Wannier-states of miniband v, are presented. Knowing that $T_1^v\approx 0.25\ W_{MB}^v$, where W_{MB}^v is the bandwidth v, one can get more information about the SL band structure using WF rather than RSM, where the single states from only one period of SL can be observed.

Table 1
Minibands and quantum states basic parameters, computed with RSM and WFM

WFM (TMF)			RSM
Miniband (v)	Energy levels the centre of minibands E^v [eV]	T_1^v [eV]	Energy levels of the quantum states [eV]
a	0.0146651	$-1.342*10^{-6}$	0.014
b	0.0291190	$4.627*10^{-5}$	0.028
c	0.0339153	$-8.128*10^{-5}$	0.033
d	0.0508985	$1.269*10^{-4}$	0.049
e	0.0622459	$-1.307*10^{-4}$	0.061

Additionally, in order to ensure the effectiveness of the calculations with the RSM, we must make sure that the Hamiltonian matrix size in this method is not too large.

In our case, it is related to the discretization of the SL structure by $a=0.6$ nm. For comparison, Bloch functions determined with the TMF have an accuracy of $a=0.1$ nm, therefore, the values of the energy levels obtained with RSM program (see Table 1), are less accurate when compared to the results obtained with the TMF method. Higher RSM accuracy requires huge Hamiltonian matrix sizes, representing the studied device, and thus either the simulation time becomes uneconomical or the computer system memory insufficient. Note that the calculations of the allowed minibands with the TMF method, with the required accuracy of $dE=1$ meV in the energy range $\Delta E=200$ meV, took about 6 minutes for a program running under Windows 7 system on the PC described above.

For calculating the Green's functions (GF), due to the WFM, we must first construct the quantum states based on the MLWF, as described elsewhere [19]. Time needed to compute MLWF, with the same hardware system, was tens minutes (according to the selected method finding MLWF [20]) for the case of 15 Wannier functions localized within an area of 20 periods of the SL, with an accuracy of $a=0.1$ nm. Because the high accuracy for energy levels, was not of much importance, the RSM gained an advantage at the start of the SL simulation.

To make a reliable comparison for GF results, the energy discretization step of 1 meV within the range 200 meV for both WFM and RSM was assumed. Computations for *structure A* were performed for $T=25$ K. The initial results of the

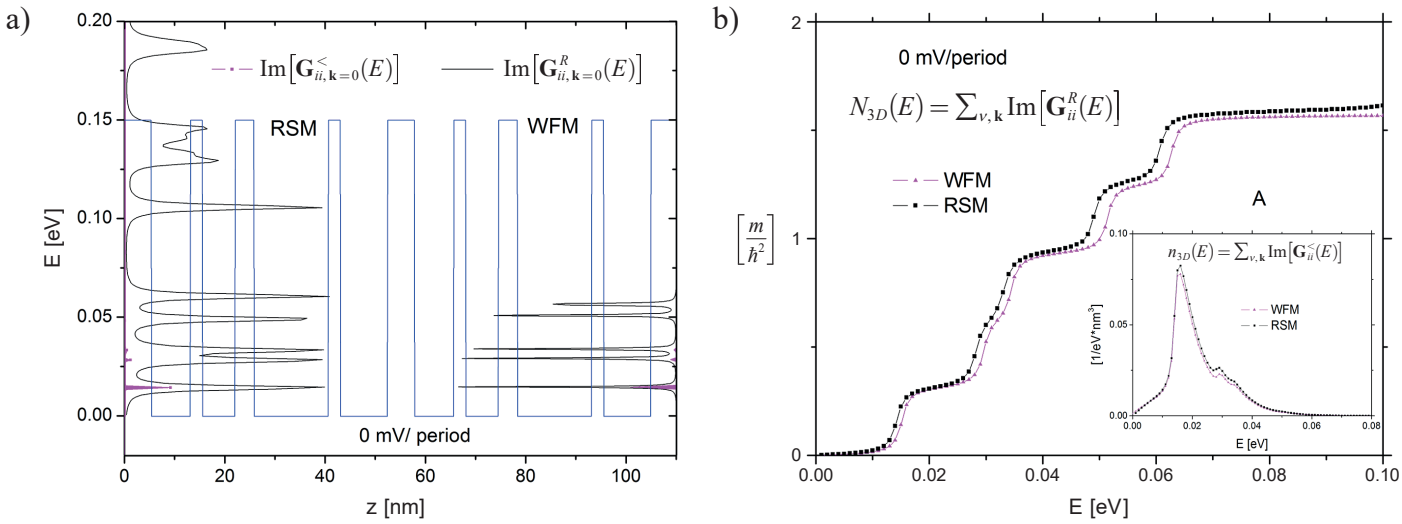

Fig. 3. Results of simulations for *structure A*: a) examples of the sum of the diagonal elements $\mathrm{Im}\left[\mathbf{G}^{R}_{ii,\mathbf{k}=0}(E)\right]$ and $\mathrm{Im}\left[\mathbf{G}^{<}_{ii,\mathbf{k}=0}(E)\right]$ as a function of the energy parameter E without the electric field; to the right – examples of these functions evaluated in the Wannier basis (WFM); to the left – examples calculated with the real space method (RSM); b) total density of states $N_{3D}(E)$ and occupation functions $n_{3D}(E)$ (inset A) in one period of the non-polarized structure, computed with WFM and RSM

NEGF computations are presented in Fig. 3a, where the sum of the diagonal elements $\mathrm{Im}\left[\mathbf{G}^{R}_{ii,\mathbf{k}=0}(E)\right]$ and $\mathrm{Im}\left[\mathbf{G}^{<}_{ii,\mathbf{k}=0}(E)\right]$ are presented as the functions of the energy parameter E without the electric field. In the right Fig. 3b, the examples of such functions, calculated in the Wannier basis are shown, whereas the left one, the example computed with the RSM may be observed. For these computations, were assumed the constant values of parameter η (i.e., $\eta = 1$ meV). In this case, the GF calculation time was short for both methods. Precisely, it was equal to 73 s, and 186 s, for the WFM and RSM (by $a = 0.6$ nm), respectively. Still, with the increased computation accuracy in the RSM, the GF calculations for $a = 0.2$ nm lasted 5200 s, whereas for an attempt to perform the simulations with the accuracy of $a = 0.1$ nm, the computer system memory was insufficient.

The Green's functions in the right Fig. 3a have five peaks, what corresponds to the same number of quantum states occurring in the structure for the considered range of energy. In the left Fig. 3a there are more peaks associated with the quantum levels. At first glance, it may seem similar to the less accurate WFM, though in this case the visible differences can be attributed to the Hamiltonian in the WFM, which included five Wannier states per period, and thus we can observe five peaks of the $\mathrm{Im}\left[\mathbf{G}^{R}_{ii,\mathbf{k}}(E)\right]$. In contrast RSM allows to determine directly nine quantum states, what corresponds to the same number of peaks of the $\mathrm{Im}\left[\mathbf{G}^{R}_{ii,\mathbf{k}}(E)\right]$ function. Herein, the number of peaks is a consequence of the considered energy range. The WFM allows to include in the Hamiltonian an arbitrary number of quantum states. In paper [13] the authors proposed four ground states and one excited state (a total number of five states) to be taken into account and they showed that this number of states is enough for the correct transport simulation.

Apart from the differences in the number of peaks for $\mathrm{Im}\left[\mathbf{G}^{R}_{ii,\mathbf{k}=0}(E)\right]$, their positions within the energy domain, obtained with both methods, are very similar for all first five states. It supports sufficient accuracy of the simulations with the RSM for the mesh size $a = 0.6$ nm.

The functions $\mathrm{Im}\left[\mathbf{G}^{<}_{ii,\mathbf{k}=0}(E)\right]$ represented in Fig. 3a with magenta lines show minor differences, as the assumed constant parameter η yielded similar self-energies values $\mathbf{\Sigma}^{<}$ for both methods. For the RSM, a linear change in the Fermi level along the SL structure was assumed, whereas for the WFM it was designed as a step function for each state.

The sum of the diagonal elements $\mathrm{Im}\left[\mathbf{G}^{<}_{ii,\mathbf{k}=0}(E)\right]$ is referred to as 1D-DOS function. By summing up the k parameter, 3D-DOS function can be obtained according to the relation $N_{3D}(E) = \sum_{\nu,\mathbf{k}} \mathrm{Im}\left[\mathbf{G}^{R}_{ii,\mathbf{k}}(E)\right]$. It was shown in Fig. 3b, where 3D-DOS functions computed with the WFM and the RSM are presented. It can be observed that these methods are convergent in the initial range of energy, although a small difference is noticeable above 60 meV. It was attributed to the greater number of the $\mathrm{Im}\left[\mathbf{G}^{R}_{ii,\mathbf{k}}(E)\right]$ peaks for the RSM, as described in the previous paragraph.

The occupation functions per period calculated according to equation $n_{3D}(E) = 2\sum_{\nu\mathbf{k}} \mathrm{Im}\left[\mathbf{G}^{<}_{ii,\mathbf{k}}(E)\right]$ are shown in the inset A of Fig. 3b. As expected, the results obtained with the WFM and the RSM show a good convergence, and the agreement between the results of $\mathrm{Im}\left[\mathbf{G}^{<}_{ii,\mathbf{k}=0}(E)\right]$ is demonstrated.

Interesting results were achieved with the electric field applied to the SL structure. In the right Fig. 4a, the $\mathrm{Im}\left[\mathbf{G}^{R}_{ii,\mathbf{k}=0}(E)\right]$ and $\mathrm{Im}\left[\mathbf{G}^{<}_{ii,\mathbf{k}=0}(E)\right]$ functions calculated with the WMF were shown and in the left one the same functions computed with the RSM was shown. When analyzing the results, it should be kept in mind that the Hamiltonian in WFM contained three adjacent superlattice periods, whereas the RSM Hamiltonian covered only one period. Applying the multi-quantum well model to RSM provides for the partial influence of the adjacent periods to be taken into account in NEGF calculations, what does not allow peaks representing the states of the neighboring periods to

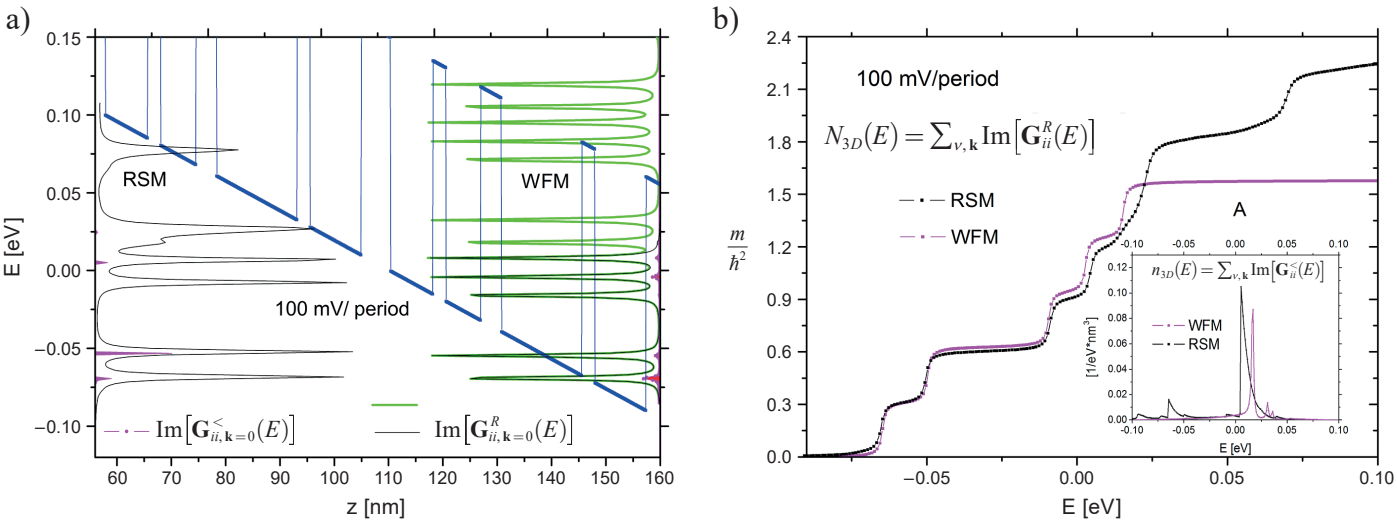

Fig. 4. Results of simulations for *structure A*: a) examples of the diagonal elements $\mathrm{Im}\left[\mathbf{G}^{R}_{ii,\mathbf{k}=0}(E)\right]$ and $\mathrm{Im}\left[\mathbf{G}^{<}_{ii,\mathbf{k}=0}(E)\right]$ and (in magenta) as function of the energy parameter E, with bias (100 mV/period) applied; to the right – exemplary functions calculated in the Wannier basis (WFM) from three periods (in green) and one selected period (in black); to the left – the same exemplary functions calculated with RSM; b) total density of states states $N_{3D}(E)$ and 3D occupation functions $n_{3D}(E)$ (inset A) in one period of the polarized structure, computed with WFM and RSM

be seen between the peaks of GF. For WFM, however, the situation is different as in the GF charts, the mixed peaks from the states of the three neighboring periods are observed (the function plotted in green). Therefore, with the electric field applied in Fig. 4a, one can see a lot more peaks function 1D DOS calculated using the WFM, than for the same function calculated with the RSM. However, we can select peaks of the 1DOS functions from a single period (see the function plotted in black) and then compare 1DOS features for both methods. The positions of the peaks are slightly displaced, what may result from not including the impact of states of neighboring periods in the RSM.

Different methods for calculating self-energies $\mathbf{\Sigma}^{<}$ for the biased structure cause discrepancies, which occur in the results of $\mathrm{Im}\left[\mathbf{G}^{<}_{ii,\mathbf{k}=0}(E)\right]$ (see graphs in magenta in Fig. 4a. It has also led to different 3D occupation functions – $n_{3D}(E)$, presented in inset A of Fig. 4b. This figure shows also 3D-DOS functions $N_{3D}(E)$ obtained with the WFM and the RSM. A smaller number of 3D-DOS steps for the WFM, when compared to RSM can be seen there. It is attributed to fewer peaks of 1D-DOS for the WFM results (see Fig. 4a): the effect may be observed when the diagonal elements $\mathrm{Im}\left[\mathbf{G}^{R}_{ii,\mathbf{k}=0}(E)\right]$ and the parameter k are summed up.

In further simulations, LO-phonon scattering processes were included by applying the Born approximation. The simulation efficiency for this case is representative for overall calculations including a self-consistent solution of the Dyson and the Keldysh equations procedure, as well as self-energy equations. Such simulations last longer. The higher the number of loop iterations is, the longer it takes to simulate, as the Hamiltonian matrix size is greater. On the other hand, some approach related differences are observed for the expressions (12–17) while computing the self-energies with the RSM and the WFM methods. Two balanced factors contribute to the effectiveness of both methods. To investigate this issue, the computations were performed with the same PC. WFM iteration loop lasted 3250 s, whereas for RSM it lasted 2880 s. Although it was found a bit surprising, it was attributed to a larger number of numerical operations required for the WMF in comparison to the RSM while computing the $\mathbf{\Sigma}^{R}$ and $\mathbf{\Sigma}^{<}$.

Such calculations can be simplified, as suggested elsewhere [12], by applying the constant momenta $\mathbf{k}_{\mathrm{typ}}$ and $\mathbf{k}'_{\mathrm{typ}}$ (and the corresponding energies E_{typ} and E'_{typ}) to evaluate the scattering matrix elements $V^{ph}_{\alpha_i\beta}(\mathbf{k}, \mathbf{k}')$. Although it diametrically accelerates simulation for the WFM, we did not use tricky ones. In the conclusion of this paragraph, it should be added, that RSM computations were performed with rather large mesh size ($a = 0.6$ nm), for a higher accuracy, computer system memory was insufficient.

The results of the simulations of the LO-phonon scattering process can be observed in Fig. 5. In this figure, the functions the $N_{3D}(E)$ and the $n_{3D}(E)$ (in inset A) obtained with the WFM and the RSM are shown. These results display differences between the methods, especially for the higher energy range, which were expected due to reasons similar to results in Fig. 4. The differences in the results for the RSM and the WFM, shown in Fig. 5a may have contributed to the differences in the results visible in Fig. 5b, where the k-resolved occupation functions $n(E, k_{\parallel})$ are presented.

The WMF allows to choose the base of the quantum states, to determine the Hamiltonian. This was shown by Lee et al. [13], who presented the use of three bases of quantum states in the QCL simulations. This allows to adjust the base of quantum states, with respect to targeted simulation results. For example, to analyze the spatial and energy location of quantum states for a biased SL structure, it is convenient to use the Wannier-Stark base.

The simulations obtained with the WFM in the Wannier-Stark base are shown in the Fig. 6a,c and the results com-

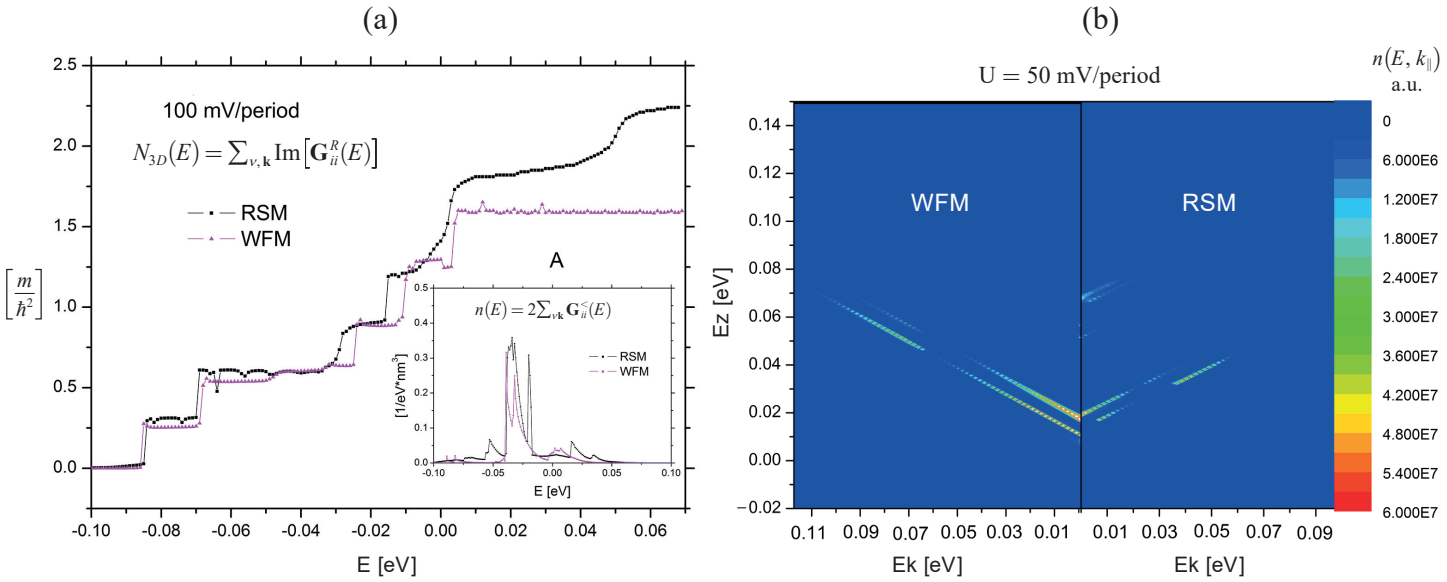

Fig. 5. Results of simulations for *structure A*: a) Total density of states – $N_{3D}(E)$ and 3D occupation functions $n_{3D}(E)$ (within A) as well as k-resolved occupation functions $n(E, k_{\|})$ (see chart b) in one period, calculated with WFM and RSM (LO-phonon process scattering on)

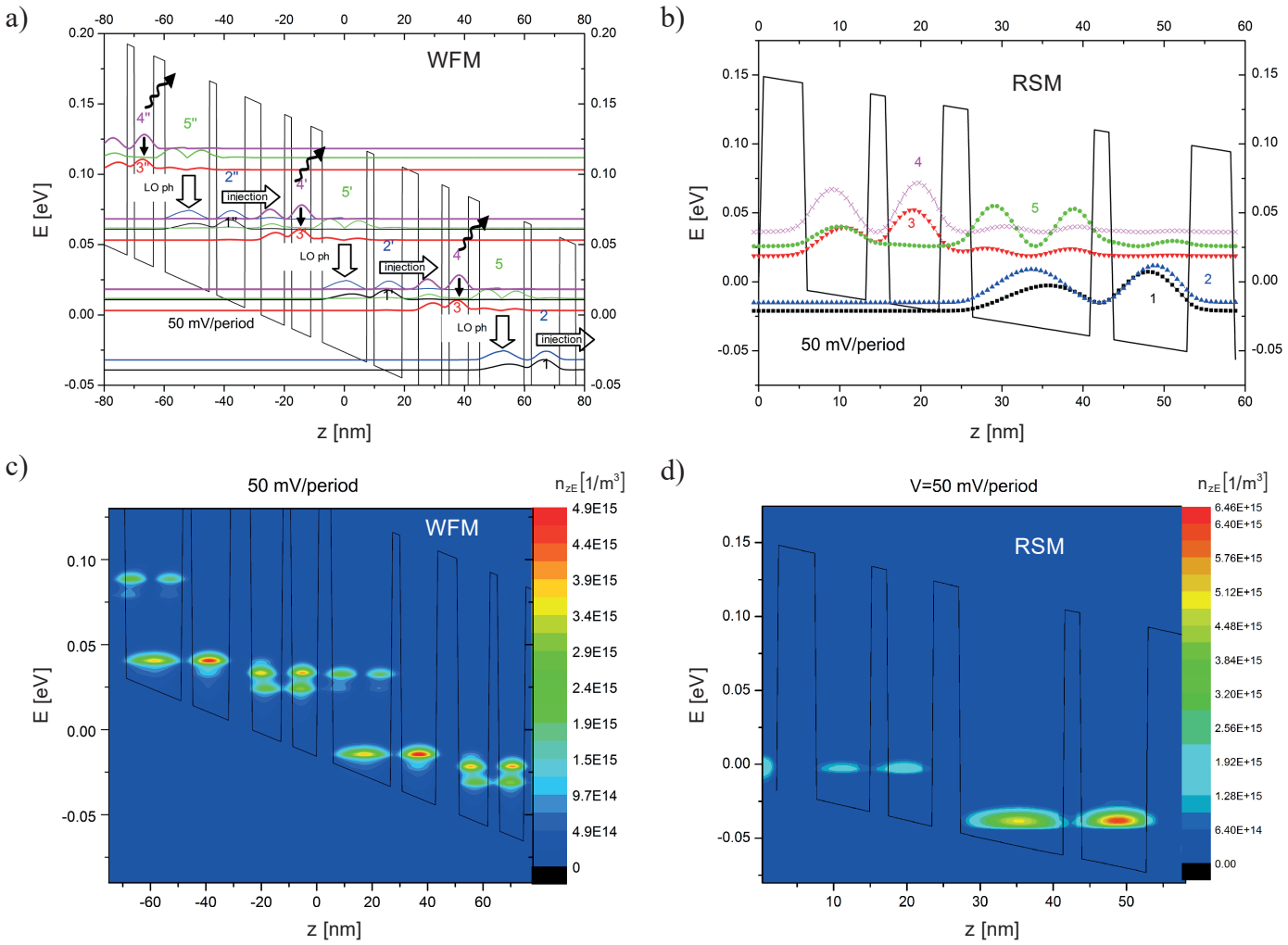

Fig. 6. a) Wannier-Stark states in three periods of *structure A* calculated with the WFM; b) Wannier-Stark states in one period of *structure A* obtained directly from RSM; c) and d) spatial-resolved densities of electrons $n(z, E)$ in *structure A*, calculated with the WFM and the RSM respectively

puted directly from the RSM can be observed in Fig. 6b, d. The calculations were performed for a constant value of the parameter η (see equation (8)).

Undoubtedly, it is a big advantage of the WFM that considering three periods of the structure allows to illustrate the transport mechanisms within the QCL much clearer than the RSM. The conclusion is supported with Fig. 6a, where the cascade of electrons flowing through the adjacent periods of the laser structure is shown.

On the other hand, Wannier–Stark states (WSS) are known to be the quantum states in a biased structure. The WFM requires quantum states to be constructed on the basis of the MLWF, as described earlier in this section. The obtained quantum states can be interpreted as the probability of finding electrons within the SL structure of energies, corresponding to specific minibands. This, however, is true for the non-biased structure. When the shape of the quantum states in the biased structure is determined, it is necessary to diagonalise the Hamiltonian in the energy representation, and then multiply the resulting transition matrix by Wannier base. Presented transformation of states may raise the questions about the accuracy of the final results, particularly with regard to the RSM, where WSS are obtained directly. Analyzing the data presented in Fig. 6. can prove helpful. It would appear that the results for both methods are very similar, particularly with regard to the shape and the position of each state within a single period; however, more detailed analysis shows slight differences in energy levels of WSS to occur. In the Fig. 6c, d, spatial-resolved densities of electrons $n(z, E)$ simulated with both method, are shown. In the WFM, it was calculated according to the relation [33]

$$n(z,E) = \frac{2}{A}\sum_{\alpha\beta\mathbf{k}} \frac{1}{2\pi i} G^{<}_{\beta\alpha}(\mathbf{k},E) WS^{*}_{\alpha}(z) WS_{\beta}(z), \qquad (18)$$

where A is the total area in (x, y) -plane, $WS^{*}_{\alpha}(z)$ and $WS_{\beta}(z)$ are the Wannier-Stark states, which are the eigenstates of $\hat{H}_0$. In the RSM, the formula for the electron density takes the following form [27]

$$n(z,E) = \frac{-2i}{aA}\sum_{\mathbf{k}}\int \frac{dE}{2\pi} G^{<}(z,z,\mathbf{k},E). \qquad (19)$$

The results show that the larger area of simulations for the WFM (when compared to the RSM) allows to observe the possibilities of electron transitions between the periods of the structure more precisely.

We get the most benefits from using the WFM, when it is necessary to simulate a structure with many narrow potential barriers in one period. In Fig. 7, results of simulations for the SL structure used in QCL [24, 25] are shown. In Fig. 7a we can see the Wannier-Stark states in three periods of the SL calculated with the WFM. In Fig. 7b the Wannier-Stark states in one period of the SL obtained directly from the RSM are plotted. The higher potential barriers of the *structure B* than the *structure A* and its more complicated construction, required a much larger amount of memory for the RSM Hamiltonian. Therefore the calculations presented in Fig. 7b lasted for a very long time, depending on the included processes of scattering. They can last from several hours to several days. After applying the WFM, the basic parameters of quantum states in the SL, were obtained after a short time (about a few minutes), additionally they concerned a larger SL area and contained more points of mesh for the one period.

Within this study, we also compared of I–V SL characteristics, simulated with the described methods, to other literature data. Fig. 8 presents the measured data for the considered QCL structure [23] and our computations (WFM with Büttiker probes

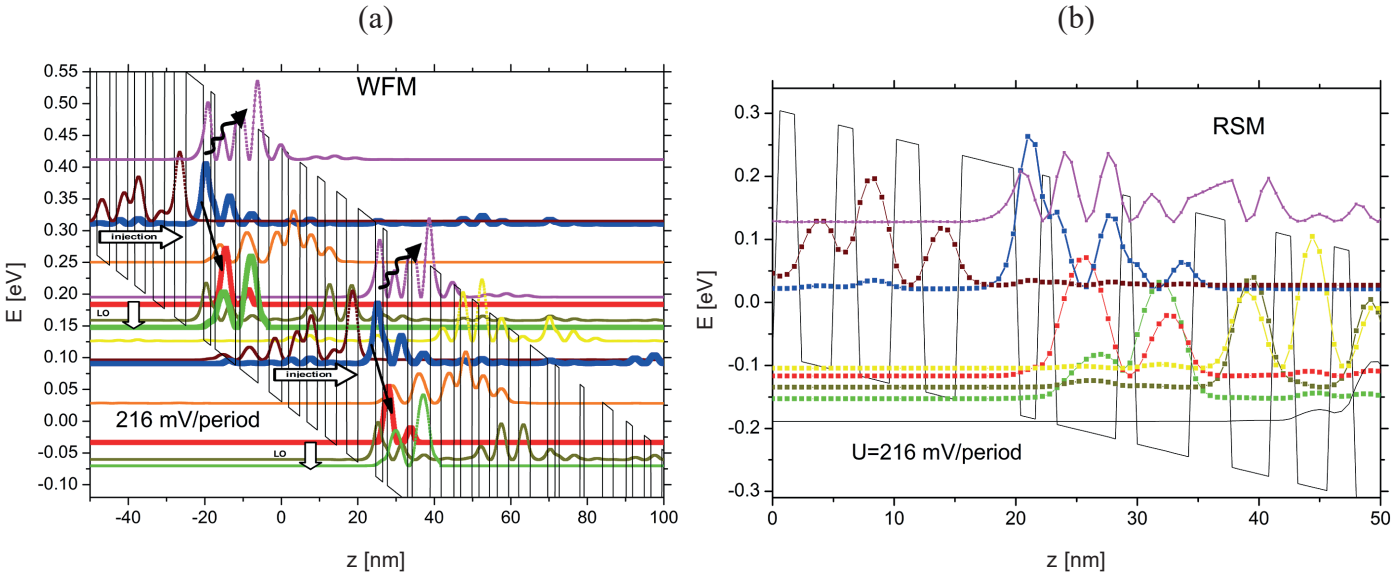

Fig. 7. Results of simulations for *structure B*: a) Wannier-Stark states in three periods of SL calculated with WFM; b) Wannier-Stark states in one period of SL obtained directly from RSM

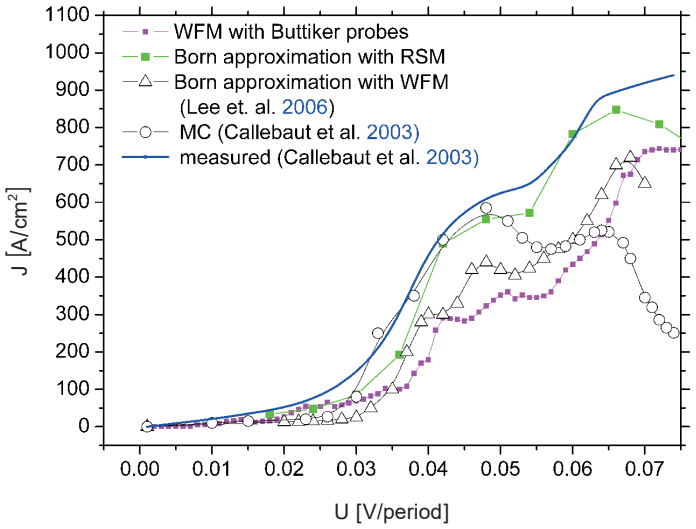

Fig. 8. Current-voltage characteristics of the SL structure [23] obtained for different approaches. The measured current-voltage characteristics of the studied structure are plotted in blue solid line

[21] and RSM with Born approximation), as well as the results obtained with Monte Carlo Method and WFM with Born approximation applied. Density of the current flowing through the SL structure, was defined for WFM as [13]

$$J = \frac{2e}{\hbar A} \sum_{\alpha,\beta,\mathbf{k}} \int \frac{dE}{2\pi} \left[\hat{H}_0, \hat{z}\right]_{\alpha,\beta} G^{<}_{\alpha,\beta,\mathbf{k}}(E), \tag{20}$$

where the matrix $\left[\hat{H}_0, \hat{z}\right]$ is formed in the Wannier-Stark base. In the RSM the current can be written as [26]

$$J = \frac{2e}{\hbar A} \sum_{\mathbf{k}} \int \frac{dE}{2\pi} \sum_{z_1 \le z} \sum_{z_2 > z} 2\mathrm{Re}\left\{\mathrm{tr}\left[t_{z_1;z_2} G^{<}(z_2, z_1, \mathbf{k}, E)\right]\right\}, \tag{21}$$

where J is the current crossing the plane between the layer z and $z+1$, e is the electron charge, while the factors of 2 are for spin degeneracy. In the equation (20), we use a block matrix notation for t and $G^{<}$, and $\mathrm{tr}\{....\}$ indicates a trace over the orbital indices in the nearest neighbor tight-binding models.

Results in the Fig. 8 show, that our numerical results did not significantly differ from the simulations published previously, but most importantly applying WFM with Büttiker probes allowed us to get 50 points I-V characteristics in a few hours, whereas computing 20 points of the same characteristics with RSM lasted several days (in both cases, the same PC was employed).

6. Summary and conclusions

Software modules in C++ were developed to implement an effective method for semiconductor superlattices simulations, which is known as the Wannier function method. The efficiency and the accuracy of the SL structure modeling have been tested with respect to the application implemented already, named as RSM. In this method due to the large size of the Hamiltonian matrix, these simulations were expected to take longer in comparison to the WFM. For modeling, a simple THz laser structure, with a mesh size of 0.6 nm for discretization of structure in the RSM, has proved to be sufficient to obtain convergent results from the WFM. Then a higher computation accuracy caused a significant decrease of the RSM effectiveness. As in the RSM Hamiltonian covers more stationary states data for the simulated structure than the Hamiltonian in the WMF, this method proved to be more convenient to use and more effective in terms of the computation time, only for the smaller number of mesh points, discretizing superlattice. As demonstrated by the numerical experiments, the maximum Hamiltonian matrix size should be of the order of several dozens, unless a very efficient computer hardware is available to perform SL simulations. Hence, the WFM is recommended for SL simulations of complicated structures, as it takes shorter time to obtain results, and huge computer memory is not required. However, in this method, the transformation of quantum states from a spatial to energy representation proves to be a simplification, due to which differences occur, when the results are compared to the RSM computations. It is especially true for higher voltage and upper energy ranges. Therefore, it seems reasonable to take proper care when interpreting results obtained with the WFM, particularly, when in the considered energy range GF peaks from three neighboring superlattice periods appear. On the other hand, inclusion three periods of the superlattice into the WFM allows to observe the effect of mixing the quantum states between the adjacent periods of the structure. We have also demonstrated certain SL parameters to be fast computable, provided that some specific simplifications in both RSM and WFM are applied. In this respect, WFM proved to open more opportunities for cascade-current observed in the device.

Acknowledgment. The work was supported by Rzeszow University of Technology, Department of Electronics Fundamentals Grant for Statutory Activity (DS 2019).

References

[1] J. Faist, F. Capasso, D.L. Sivco, A.L. Hutchinson, S-N.G. Chu, and A.Y. Cho, "Short wavelength ($\lambda \sim 3.4$ μm) quantum cascade laser based on strained compensated InGaAs/AlInAs", *Appl. Phys. Lett.*, 72, 680–684 (1998).

[2] R. Colombelli, F. Capasso, C. Gmachl, A.L. Hutchinson, D.L. Sivco, A. Tredicucci, M.C. Wanke, A.M. Sergent, and A.Y. Cho, "Far infrared surface-plasmno quantum-cascade lasers at 21.5 μm and 24 μm wavelenglengths", *Appl. Phys. Lett.*, 78, 2620–2622 (2001).

[3] K. Kosiel, M. Bugajski, A. Szerling, J. Kubacka-Traczyk, P. Karbownik, E. Pruszyńska-Karbownik, J. Muszalski, A. Łaszcz, P. Romanowski, M. Wasiak, W. Nakwaski, I. Makarowa, and P. Perlin, "77 K Operation o AlGaAs/GaAs Quantum Cascade Laser at 9 μm", *Photonics Lett. Pol.*, 1 (1) 16–18 (2009).

[4] R.F. Kazarinov and R.A. Suris, "Possibility of the Amplification of Electromagnetic Waves in a Semiconductor with a Superlattice", *Sov. Phys. Semicond.* 5, 707–709 (1971).

[5] M. Bugajski, K. Pierściński, D. Pierścińska, A. Szerling, and K. Kosiel, "Multimode Instabilities in Mid-Infrared Quantum Cascade Lasers", *Photonics Lett. Pol.*, 5 (3) 85–87 (2013).
[6] P. Karbownik, A. Trajnerowicz, A. Szerling, A. Wójcik-Jedlińska, M. Wasiak, E. Pruszyńska-Karbownik, K. Kosiel, I. Gronowska, R. P. Sarzała, and M. Bugajski, "Direct Au-Au Bonding Technology for High Performance GaAs/AlGaAs Quantum Cascade Lasers", *Opt. Quant. Electron.*, 47 (4) 893–899 (2015).
[7] E. Bellotti, K. Driscoll, T.D. Moustakas, and R. Paiella, "Monte Carlo simulation of terahertz quantum cascade laser structures based on wide-bandgap semiconductors", *J. Appl. Phys*., 105 (11) 113103–113103–9 (2009).
[8] P. Borowik, J.L. Thobel, and L. Adamowicz, "Monte Carlo modeling applied to studies of quantum cascade lasers", *Opt. Quant. Electron.*, 49: 96 (2017).
[9] T. Kubis, C. Yeh, and P. Vogl, "Theory of nonequilibrium quantum transport and energy dissipation in terahertz quantum cascade lasers", *Phys. Rev. B*, 79 (19) 195323–1–195323–10, May (2009).
[10] A. Wacker, "Gain in quantum cascade lasers and superlattices: A quantum transport theory", *Phys. Rev. B*, 66, 085326–1–085326–7 (2002).
[11] M. Pereira, S-C Lee, and A. Wacker, "Effect of Coulomb corrections and mean field on gain and absorption in Quantum Cascade Lasers", *Phys. Status Solidi C*: current topics in Solid State Physics, 2 (8), 3027–3030 (2005).
[12] S.-C. Lee and A. Wacker, "Nonequilibrium Green's function theory for transport and gain properties of quantum cascade structures", *Phys. Rev. B*, 66, 245314–1– 245314–18 (2002).
[13] S.-C. Lee, F. Banit, M. Woerner, and A. Wacker, "Quantum-mechanical wavepacket transport in quantum cascade laser structures", *Phys. Rev. B*, 73, 245320–1–245320–6, (2006).
[14] S. Birner, T. Zibold, T. Andlauer, T. Kubis, M. Sabathil, A. Trellakis, and P. Vogl, "Nextnano: General Purpose 3-D Simulations", *IEEE Transactions on Electron Devices*, 54 (9) 2137–2142 (2007).
[15] G. Hałdaś, A. Kolek, and I. Tralle, "Modeling of Mid-Infrared Quantum Cascade Laser by Means of Nonequilibrium Green's Functions", *IEEE J. Quantum Electron.*, 47 (6) 878–885 (2011).
[16] G. Hałdaś, A. Kolek, D. Pierścińska, P. Gutowski, K. Pierściński, P. Karbownik, and M. Bugajski, "Numerical simulation of GaAs-based mid-infrared one-phonon resonance quantum cascade laser", *Opt. Quant. Electron*., 49, 22 (2017).
[17] A. Kolek, G. Hałdaś, and M. Bugajski, "Nonthermal Carrier Distributions in the Subbands of 2-Phonon Resonance Mid-Infrared Quantum Cascade Laser", *Appl. Phys. Lett.*, 101, 061110 (2012).
[18] M. Mączka, S. Pawłowski, and J. Plewako, "Comparative analysis of selected models of semiconductor superlattices", *Przegląd Elektrotechniczny*, no. 8, 93 (2011).
[19] M. Mączka, S. Pawłowski, "Wannier function applied to quantum cascade lasers modelling", *Przegląd Elektrotechniczny*, no. 12, 245–249 (2013).
[20] M. Mączka, G. Hałdaś, and S. Pawłowski, "Study of quantum states maximal localization in nonsymmetrical semiconductor superlattice structures", *Selected Issues of Electrical Engineering and Electronics* (WZEE), IEEE Conference Publications, 13 (2016).
[21] M. Mączka, "Calculations of the QCL transport parameters using Büttiker probes", *Przegląd Elektrotechniczny*, no. 7, 190–196 (2016).
[22] M. Mączka and S. Pawłowski, "Efficient method for transport simulations in quantum cascade lasers", International Conference on Semiconductor Nanostructures for Optoelectronics and Biosensors (IC SeNOB), *EPJ Web of Conferences*, 133 (2017).
[23] H. Callebaut, S. Kumar, B.S. Williams, and Q. Hu, "Analysis of transport properties of tetrahertz quantum cascade lasers", *App. Phys. Lett.* 83 (2) 207–209 (2003).
[24] H. Page, C. Becker, A. Robertson, G. Glastre, V. Ortiz, and C. Sirtori, "300 K operation of a GaAs-based quantum-cascade laser at $\lambda \approx 9$ μm", *App. Phys. Lett.* 78, 3529–3531 (2001).
[25] A. Wacker, "Semiconductor superlattices: a model system for nonlinear transport", *Physics Reports*, 357, 1–111 (2002).
[26] R. Lake, G. Klimeck, R. C. Bowen, and D. Jovanovic, "Single and multiband modeling of quantum electron transport through layered semiconductor devices", *J. Appl. Phys.*, 81, 7845–7869 (1997).
[27] S. Datta, "Steady-state quantum kinetic equation", *Phys. Rev. B*, 40, 5830–5833 (1989).
[28] S. Datta, *Electronic transport in mesoscopic systems*, Cambridge University Press, 1995.
[29] S. Datta, "A simple kinetic equation for steady-state quantum transport", *J. Phys. Condens. Matter*, 2 (40) 8023 (1990).
[30] L.V. Keldysh, "Diagram technique for non-equilibrium processes", *Sov. Phys. JETP*, 20 (4) 1018–1026 (1965).
[31] M. Büttiker, "Four-Terminal Phase-Coherent Conductance", *Phys. Rev. Lett.*, 57, 1761–1764 (1986).
[32] R. Venugopal, M. Paulsson, S. Goasguen, S. Datta, and M. Lundstrom, "A simple quantum mechanical treatment of scattering in nanoscale transistors", *J. Appl. Phys*., 93, 5613–5625 (2003).
[33] A. Wacker, "Coherence and spatial resolution of transport in quantum cascade lasers", *Phys. Stat. Sol.*, 5 (1) 215–220 (2008).